Unviersty of Anbar

Anbar Journal Of Engineering Science©

journal homepage: http:// http://www.uoanbar.edu.iq/Evaluate/

# Numerical Study on Hydrothermal Performance Factor Using Jet impingement and Nanofluid

**Ibrahim K. Alabdaly [a], M. A. Ahmed [b*]**

[a, b] *Dept. of Mechanical Engineering, College of Engineering, University of Anbar, Ramadi, Iraq*

**PAPER INFO**

***Paper history:***
Received … … …
Received in revised form … … …
Accepted … … …

***Keywords:***
Jet Impingement, Thermal-hydraulic performance, Nanofluids, Laminar flow, Finite volume method.

**ABSTRACT**

In this study, thermal-hydraulic performance of a confined slot jet impingement with $Al_2O_3$-water nanofluid has been numerically investigated over Reynolds number ranges of 100-1000. Two triangular ribs are mounted at a heated target wall; one rib located on the right side of the stagnation point and another one located on left side of the stagnation point. The governing momentum, continuity and energy equations in the body-fitted coordinates terms are solved using the finite volume method and determined iteratively based on SIMPLE algorithm. In this study, effects of Reynolds number, rib height and rib location on the thermal and flow characteristics have been displayed and discussed. Numerical results show an increase in the average Nusselt number and pressure drop when Reynolds number and rib height increases. In addition, the pressure drop and average Nusselt number increases with decrease the space between the stagnation point and rib. The maximum enhancement of the average Nusselt number is up to 39 % at Reynolds number of 1000, the rib height of 0.3, rib location of 2 and nanoparticles volume fraction of 4%. The best thermal-hydraulic performance of the impinging jet can be obtained when the rib height of 0.2 and rib location of 2 from the stagnation point with 4% nanoparticles volume fraction.

© 2014 Published by Anbar University Press. All rights reserved.

## 1. Introduction

Among many convection transport methods, jet impingement considered an attractive method especially in cooling or heating systems because of the high heat transfer rates. Therefore, the impinging jet technique is widely employed in different industrial applications such as cooling of electronic equipment, turbine blades, glass tempering, metal annealing and paper drying [1,2].

There are many experimental and numerical investigations on the jet impingement. A confined air jet impingement on the flat channel have experimentally and numerically investigatd by Hee et al. [3] as well as Sahoo and Sharif [4]. Their results showed that the maximum heat transfer rate at the stagnation point. Dagtekin and Oztop [5] numerically investigated on the double slot-jets impingement and the results showed that the average Nusselt number increases linearly with increasing Reynolds number and the influence of Reynolds number on skin friction was significant around the impingement zone. Choo and Kim [6] performed an experimental study to compare the confined and unconfined air jets correlations for average Nusselt number. It was observed that under a constant pumping power condition, the heat transfer rates of the unconfined jet was similar to that for the confined jet. Sharif [7] numerically investigated of the air slot-jet impingement on heated plate. Results noted that the skin friction and Nusselt number increased with decreasing the jet-to-plate spacing. Simionescu et al. [8] carried out an experimental and numerical investigation to study the heat transfer enhancement using air jet impingement and it is found that the static wall pressure increased with increasing Reynolds number. Barik et al. [9] numerically investigated on the thermal field using a

* Corresponding author. Tel.: +964-7831054434
*E-mail address: mohammed.abed@uoanbar.edu.iq*

rectangular channel with various surface protrusion by cross-flow jet. Three different protrusion such as trapezoidal, triangular and rectangular shapes have been presented. It is found that the triangular protrusion shape displyas the best heat transfer rate but with the higher pressure drop.

Using the jet impingement with dimples surface to increase the heat transfer rates was studied by many investigators [10,11 and 12]. They showed the heat transfer rate enhanced with using dimples surface as a compared to flat plate. Casanova and Ortiz [13] investigated on the effect of bumps and dimples surfaces on the air jet impingement to enhance heat transfer and compared with the flat plate. Gau and Lee [14] performed an experimental study on the heat transfer of air jet impingement with the triangular rib-roughened surface to enhance the heat transfer rate. Dobbertean and Rahman [15] presented the effect of the triangular rib and triangular steps shaped surfaces on the heat transfer enhancement using liquid jet impingement. Results showed that the heat transfer rates improved with height of ribs.

Manca et al. [16] conducted the numerical investigation of the turbulent jet impingement with $Al_2O_3$-water nanofluid and it is found that the mean Nusselt number increased as increasing nanoparticle concentration and Reynolds number. Forced convection flow using $Al_2O_3$-water nanofluid in a radial flow cooling system have been investigated by Palm et al. [17] as well as Yang and Lai [18]. Results showed that the Nusselt number and pressure drop increased with increasing nanoparticle volume fraction. Sun et al. [19] have been conducted an experiments to study the heat transfer of jet impingement with copper-water nanofluids and it is observed that best heat transfer enhancement obtained at the jet angle of 90°. Gherasim et al. [20] have been performed an experimental investigation on laminar convective heat transfer of $Al_2O_3$-water nanofluid flow between a heated disk and flate plate. It was noted that the mean Nusselt number enhanced with increasing nanoparticle concentration and it decreases as increasing the jet-to-disk spacing. Manca et al. [21] numerically investigated on laminar slot-jet impingement with $Al_2O_3$-water nanofluid and it was showed that the maximum Nusselt number was about 36% at nanoparticles concentration of 0.05.

In the present study, a laminar forced convention of a confined impinging slot-jet on a heated plate with triangular ribs using nanofluid is numerically investigated for Reynolds number range of 100-1000 and nanoparticles volume fraction of 4%. The effects of Reynolds number, the rib heights and the distance between the rib and the stagnation point on the thermal and flow characteristics have been displayed and discussed.

## 2. Mathematical Formulation

### *2.1. Problem description*

**Figure 1** shows the geometrical configuration of a confined slot-jet impingement. The jet width (w) is 10 mm, the distance between the jet and the target plate is (H), and the length of the target plate is L=200 mm. Two triangular ribs with height of (a) are mounted at the target plate; one rib located right the stagnation point while another one located left the stagnation point. The distance between the rib and the stagnation point is (b). For the current study, the following geometric parameters are applied; H/W= 1, a/W=0.0, 0.15, 0.2 and 0.3 as well as b/W=1, 2, 3 and 4. The assumptions of this study are: laminar flow, steady state, incompressible fluid and two-dimensional as well as the mixture of nanoparticles and water is homogeneous. The diameter of the spherical nanoparticles is 30 nm. Because of the physical domain is symmetric about the y-axis, only the half-domain is considered in this study.

### *2.2. Governing equations*

The non-dimensional governing equations in the body-fitted coordinate are [22]:

Continuity equation:

$$\frac{\partial U^C}{\partial \zeta} + \frac{\partial V^C}{\partial \eta} = 0 \tag{1}$$

X-Momentum:

$$\frac{\partial}{\partial \zeta}\left(UU^C\right) + \frac{\partial}{\partial \eta}\left(UV^C\right) = \frac{-\partial}{\partial \zeta}\left(Y_\eta P\right) + \frac{\partial}{\partial \eta}\left(Y_\zeta P\right) + \frac{1}{Re}\left[\frac{\partial}{\partial \zeta}\left(\beta_{11}\frac{\partial U}{\partial \zeta}\right) + \frac{\partial}{\partial \eta}\left(\beta_{22}\frac{\partial U}{\partial \eta}\right) + \frac{\partial}{\partial \zeta}\left(\beta_{12}\frac{\partial U}{\partial \eta}\right) + \frac{\partial}{\partial \eta}\left(\beta_{21}\frac{\partial U}{\partial \zeta}\right)\right] \tag{2}$$

Y-Momentum:

$$\frac{\partial}{\partial \zeta}\left(VU^C\right) + \frac{\partial}{\partial \eta}\left(VV^C\right) = \frac{\partial}{\partial \zeta}\left(X_\eta P\right) - \frac{\partial}{\partial \eta}\left(X_\zeta P\right) + \frac{1}{Re}\left[\frac{\partial}{\partial \zeta}\left(\beta_{11}\frac{\partial V}{\partial \zeta}\right) + \frac{\partial}{\partial \eta}\left(\beta_{22}\frac{\partial V}{\partial \eta}\right) + \frac{\partial}{\partial \zeta}\left(\beta_{12}\frac{\partial V}{\partial \eta}\right) + \frac{\partial}{\partial \eta}\left(\beta_{21}\frac{\partial V}{\partial \zeta}\right)\right] \tag{3}$$

Energy:

$$\frac{\partial}{\partial \zeta}\left(\theta U^C\right) + \frac{\partial}{\partial \eta}\left(\theta V^C\right) = \frac{1}{Re\,Pr}\left[\frac{\partial}{\partial \zeta}\left(\beta_{11}\frac{\partial \theta}{\partial \zeta}\right) + \frac{\partial}{\partial \eta}\left(\beta_{22}\frac{\partial \theta}{\partial \eta}\right) + \frac{\partial}{\partial \zeta}\left(\beta_{12}\frac{\partial \theta}{\partial \eta}\right) + \frac{\partial}{\partial \eta}\left(\beta_{21}\frac{\partial \theta}{\partial \zeta}\right)\right] \tag{4}$$

Where:

$$U^C = UY_\eta - VX_\eta, \quad V^C = -UY_\zeta + VX_\zeta,$$
$$J = X_\zeta Y\eta - X\eta Y_\zeta, \quad \beta_{12} = \beta_{21} = -\left(X_\zeta X_\eta + Y_\zeta Y_\eta\right)/J,$$
$$\beta_{22} = \left(X_\zeta^2 + Y_\zeta^2\right)/J, \quad \beta_{11} = \left(Y_\eta^2 + X_\eta^2\right)/J \tag{5}$$

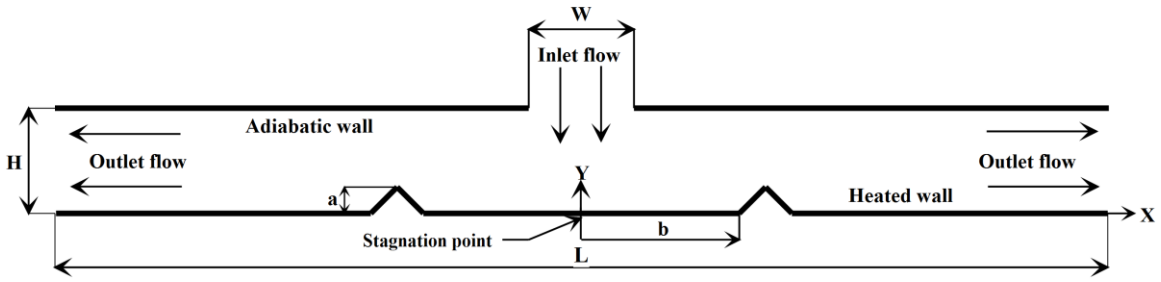


**Figure 1:** Geometry of the current study.

The non-dimensional quantities used in the previous equations are given as:

$$X = \frac{x}{W}\ ,\ Y = \frac{y}{W}\ ,\ U = \frac{u}{V_{in}}\ ,\ V = \frac{v}{V_{in}}\ ,$$

$$\theta = \frac{T - T_{in}}{T_w - T_{in}},\ P = \frac{P}{\rho_{nf}\, V_{in}^2} \quad (6)$$

### 2.3. Boundary conditions

The boundary conditions used in the current study is expressed as:

i. Jet inlet section:

$$\mathrm{U} = 0,\ \mathrm{V} = -1\ ,\ \theta = 0 \quad (7a)$$

ii. Outlet section:

$$\frac{\partial \mathrm{U}}{\partial \mathrm{X}} = 0\ ,\ \frac{\partial \mathrm{V}}{\partial \mathrm{X}} = 0\ ,\ \frac{\partial \theta}{\partial \mathrm{X}} = 0 \quad (7b)$$

iii. Target wall:

$$\mathrm{U} = 0,\ \mathrm{V} = 0\ ,\theta = 1 \quad (7c)$$

iv. Upper wall:

$$\mathrm{U} = 0\ ,\ \mathrm{V} = 0\ \ ,\ \frac{\partial \theta}{\partial \mathrm{Y}} = 0 \quad (7d)$$

v. Symmetry line:

$$\frac{\partial \mathrm{U}}{\partial \mathrm{X}} = 0\ \ ,\ \ \frac{\partial \mathrm{V}}{\partial \mathrm{X}} = 0\ \ ,\ \ \frac{\partial \theta}{\partial \mathrm{X}} = 0 \quad (7e)$$

The local and average Nusselt number at the target plate can be calculated as follow:

$$Nu_x = \frac{h_x W}{K_{nf}} = -\frac{K_{nf}}{K_{bf}}\frac{\partial \theta}{\partial Y}\ ,\ Nu_{av.} = \frac{1}{L}\int_0^L Nu_x\, dx \quad (8)$$

The friction factor can be expressed as:

$$f = \Delta P\ \frac{W}{L}\frac{2}{\rho_{nf} V_{in}^2} \quad (9)$$

The thermal-hydraulic performance factor can be defined as [23]:

$$\mathrm{PEC} = \left(\frac{Nu_{av,nf}}{Nu_{av,bf}}\right) \Big/ \left(\frac{f_{nf}}{f_{bf}}\right)^{1/3} \quad (10)$$

### 2.4. Thermophysical properties of nanofluid

i. Density and heat capacity:

The density and heat capacity of $Al_2O_3$-water is produced as [24]:

$$\rho_{nf} = (1-\varphi)\rho_f + \varphi\rho_p \quad (11)$$

$$\left(\rho\, C_p\right)_{nf} = (1-\varphi)\left(\rho\, C_p\right)_f + \varphi\left(\rho\, C_p\right)_p \quad (12)$$

ii. The dynamic viscosity:

The dynamic viscosity of nanofluid is given by [25]:

$$\frac{\mu_{nf}}{\mu_f} = \frac{1}{1 - 34.87\,(d_p/d_f)^{-0.3}\,\varphi^{1.03}} \quad (13)$$

where d$f$ is the equivalent diameter of the base fluid molecule, it can be calculated as:

$$d_f = 0.1\left[\frac{6\,M}{N\,\pi\,\rho_{fo}}\right]^{1/3} \quad (14)$$

where $\rho f_o$ is the density of the base fluid determined at the temperature of $T_o$ = 293 K.

iii. Thermal conductivity:

The effective thermal conductivity of nanofluid can be presented by [26]:

$$K_{eff} = K_{static} + K_{Brownian} \quad (15)$$

Where

$$K_{static} = K_f\left[\frac{(K_p + 2K_f) - 2\varphi(K_f - K_p)}{(K_p + 2K_f) + \varphi(K_f - K_p)}\right] \quad (16)$$

$$K_{Brownian} = 5\times 10^4\ \mathcal{B}\ \varphi\ \rho_f\ C_{pf}\ \sqrt{\frac{\kappa\, T}{\rho_p\, d_p}}\ f(T,\varphi) \quad (17)$$

$$\mathcal{B} = 1.9526\,(100\ \varphi)^{-1.4594} \quad (18)$$

$$f(T,\varphi) = (2.8217\times 10^{-2}\ \varphi + 3.917\times 10^{-3})\left(\frac{T}{T_o}\right) + (-3.0669\times 10^{-2}\ \varphi - 3.91123\times 10^{-3}) \quad (19)$$

The properties of nanoparticles and water is similar to that of Mohammed et al. [27].

## 3. Numerical Method

The governing equations in the body-fitted coordinate have been discretized using finite volume approach and solved iteratively using SIMPLE algorithm [28]. The upwind scheme is adopted to discretize the convection terms in governing equations, while the central difference scheme is employed to discretize the diffusion terms. Moreover, a collocated grid arrangement is adopted in the current study [29]. On the other hand, the differential equation method (which is relied on the Poisson equations) can be used to develop the computational mesh. Therefore, the Poisson equations solved using the finite difference method to generate the computational grid. **Figure 2** presents computational grid for the current study at a/W=0.3 and b/W=2. The under-relaxation factor is employed to obtain the best convergence and the value of convergence criterion for all variables is $10^{-5}$.

## 4. Code Validation and Grid Test

In order to verify the numerical algorithm used in this investigation, the average Nusselt number of the jet impingement confined by parallel walls was determined and compared with a numerical result of Sahoo and Sharif [4]. According to **Figure 3**, It is observed that the agreement between the results of these two studies is very good. To check the grid independence, different mesh sizes such as (101×31, 161×51, 241×71, 361×101, 421×121) are tested. **Figure 4** displays the local Nusselt number along the smooth target plate for various mesh sizes at Re = 300, φ=4%. It can be employed the fourth grid size of 361×101 as the grid independence for all results in the current study.

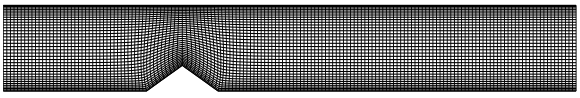

**Figure 2:** Computational Grid for the current study.

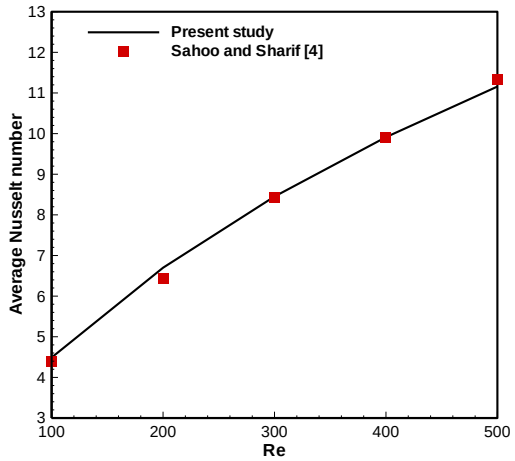


**Figure 3:** The comparison of average Nusselt number for the current study with a previous numerical study of Sahoo and Sharif [4].

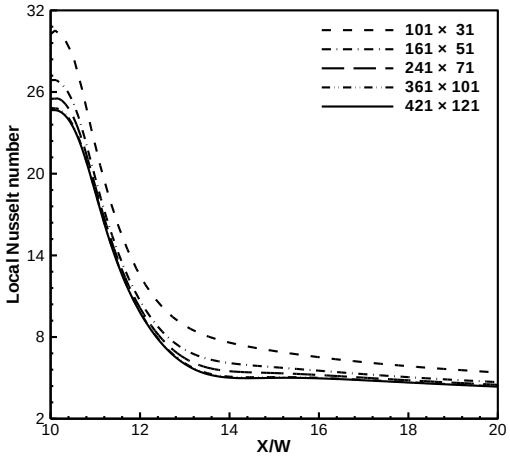


**Figure 4:** The local Nusselt number along the smooth target surface for various grid sizes at Re = 300, φ=4%.

## 5. Results and Discussion

The effects of Reynolds number, height of ribs and the distance between the stagnation point and ribs on flow and thermal characteristics are presented and discussed. The streamwise velocity contours (left) and the isotherms contours (right) at Re= 100, 500 and 1000, a/W= 0.3, b/W= 2, and φ= 4 % are shown in **Figure 5**. When a jet impinges on the target plate, a re-circulation region can be seen in the neighborhood of confinement plate and jet inlet due to the shear force induced by jet on the fluid in channel. Another re-circulation region is formed downstream the rib near the target plate and the nanofluid leaves the domain as a channel flow. At Re=1000, the size of re-circulation regions increase as well as a third re-circulation region grows at the confinement plate near the exit of channel. Looking at isotherms contours, that the minimum thermal boundary layer thickness is observed at the stagnation region due to the high velocity gradient. As Reynolds number increase, the thickness of thermal boundary layer decreases and then increase the temperature gradient near the target plate due to increase the velocity gradient at the target wall. Also it can be seen that the presence of recirculation region downstream the rib can improve the hot fluid near the target plate with cold fluid in core and hence improve the heat transfer from the target plate. This effect increase with Reynolds number due to increase the recirculation regions size.

**Figure 6** shows the prediction of the mean Nusselt number with Reynolds number for various rib heights at b/W=2 and φ=4%. For all rib heights, the average Nusselt numbers increase with Reynolds number because of the increase in the temperature gradient at the target wall. At a given Reynolds number, the mean Nusselt number increases with rising the rib heights. This is due to

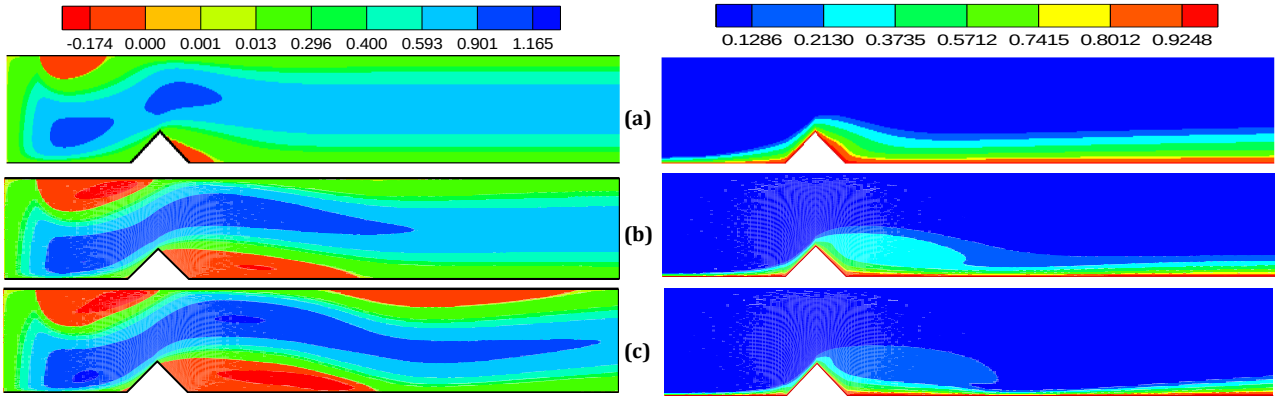


**Figure 5:** Streamwise velocity (left) and the temperature contours (right) for various Reynolds number (a) Re=100, (b) Re=500 and (c) Re=1000 at a/W=0.3 and b/W=2.

the improvement in the fluid flow mixing and hence enhance the heat transfer rates. The average Nusselt number is enhanced up to 31.2, 34.4 and 39 % for a/W= 0.1, 0.2 and 0.3, respectively at Re =1000, φ=4 % and b/W=2 compared with the smooth target plate. **Figure 7** presents the variation of pressure drop with Reynolds numbers for various rib heights at b/W=2 and φ=4%. As Reynolds number increase, the pressure drop increases for any value of rib height. It is also found that the pressure drop increases with the rib heights, especially at high Reynolds number. When ribs height increase, the size and intensity of the re-circulation regions, that formed near the target, as well as the reverse flow increases which leads to increase the pressure drop. **Figure 8** displays the variation of thermal-hydraulic performance factor with Reynolds numbers for different rib heights at b/W=2 and φ=4%. Gernerally, it can be seen that the height of the rib has a significant effect on the performance factor. The highest performance factor is achived with rib height of 0.2. Therefore, the peak value of thermal-hydraulic performance factor is about 1.9 at rib height of 0.2, Re =1000 and b/W = 2. In addition, the performance factor is lower than unity when the rib height of 0.3 and Re > 300. This indicates that the increase in pressure drop is greater than the enhancement in heat transfer. The effect of the distance between a rib and the stagnation point on the average Nusselt number at a/W=0.2 and φ=4 % is presented in **Figure 9**. It is found that the average Nusselt number increase with decreasing the distance between the rib and the stagnation point. This because of the flow becomes more disturbed and hence improves the fluid flow mixing and increases the heat transfer rates. It is also observed that there is a slight effect of rib location on the average Nusselt number at b/W=1.0 and 2.0. **Figure 10** depicts the variation of the pressure drop with Reynolds number for different distance between the rib and the stagnation point at a/W=0.2 and φ=4 %. It is observed that the pressure drop raises with decreasing the distance between the rib and stagnation point. This is because when the rib location is closer to the stagnation point, the flow becomes more disturbed and hence increase the pressure drop due to the intensity of the fluid flow is the greatest near the stagnation point.

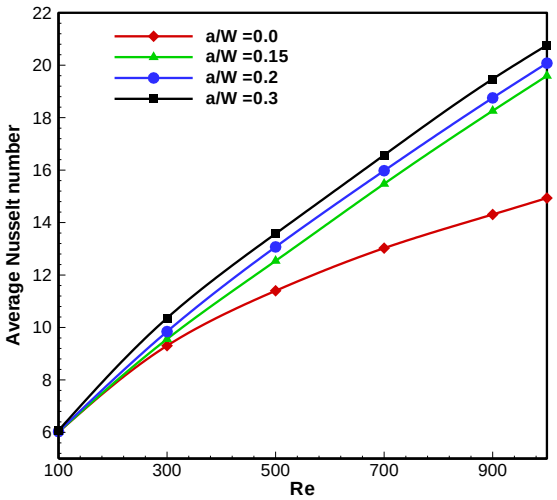


**Figure 6:** Average Nusselt number with Reynolds numbers for various rib heights at b/W=2.

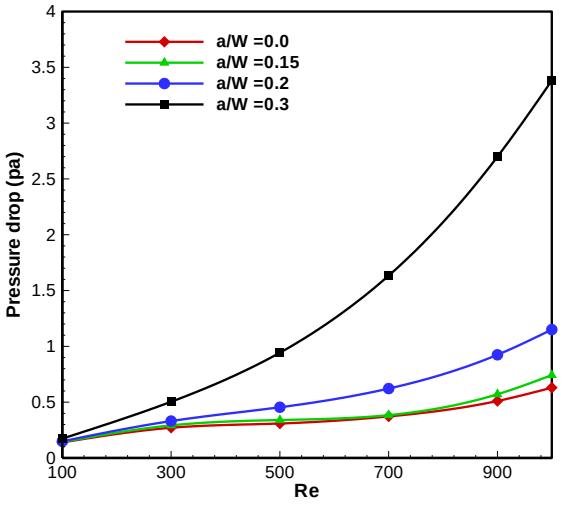


**Figure 7:** Pressure drop with Reynolds number for different rib heights at b/W=2.

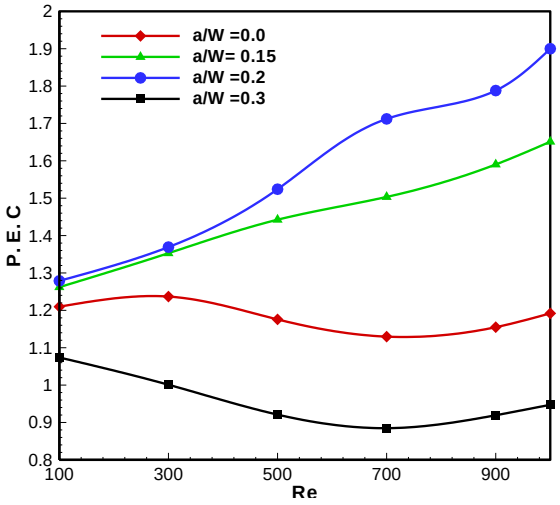


**Figure 8:** Thermal-hydraulic performance factor vs. Reynolds number for different rib heights at b/W=2.

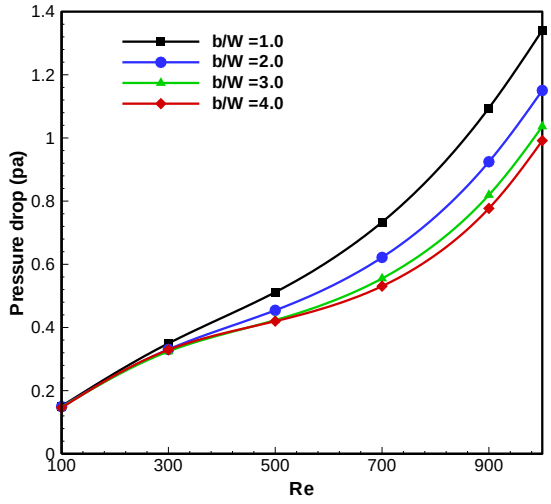


**Figure 10:** Pressure drop with Reynolds numbers for various rib locations at a/W=0.2.

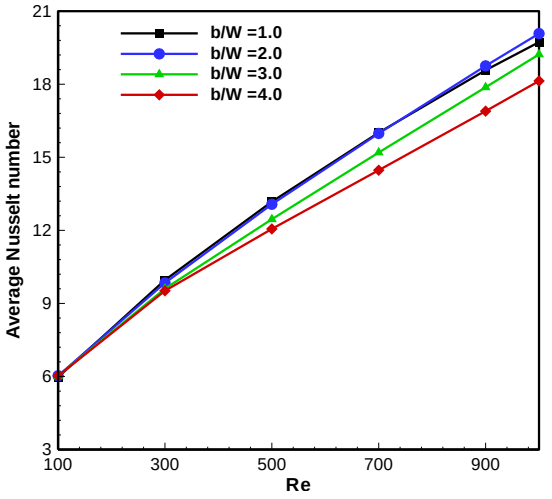


**Figure 9:** Average Nusselt number with Reynolds numbers for different rib locations at a/W=0.2.

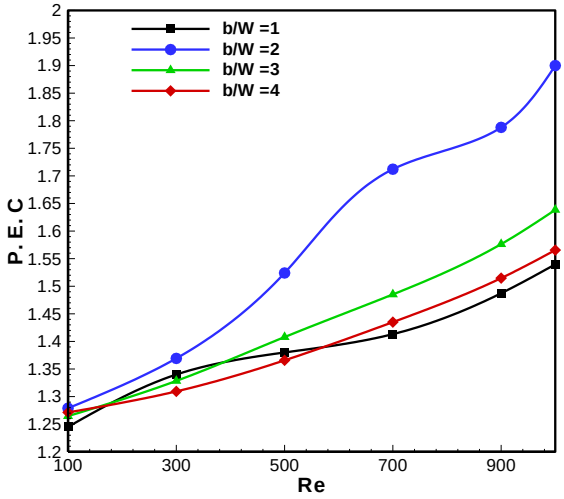


**Figure 11:** Thermal-hydraulic performance factor vs. Reynolds numbers for different rib locations at a/W=0.2.

**Figure 11** Presents the influence of rib locations on thermal-hydraulic performance at a/W=0.2 and φ=0.4 %. It can be seen that the performance factor increases with Reynolds number for any location of rib on the target wall. It is also found that the performance factor for all rib locations and Reynolds numbers are higher than unity. This is because the heat transfer enhancement is greater than the augmentation in pressure drop. The highest performance factor occurs when the rib is located at distance of 2 from the stagnation point because of the b/W = 2 has the best fluid flow mixing compared with other ribs locations. However, the peak value of performance factor is around 1.9 at b/W=2, a/W=0.2 and φ=4 %.

## 6. Conclusion

In this study, the flow and thermal characteristics of a confined slot jet impingement with $Al_2O_3$-water nanofluid has been numerically investigated. Two triangular ribs which are mounted on a target wall have been employed to enhance the heat transfer. The effect of Reynolds number, rib height and rib location on the thermal and flow fields have been displayed. It is observed that the average Nusselt number increase with Reynolds number and rib height, but this is a companied by increasing in the pressure drop. Furthermore, the average Nusselt number and the pressure drop increase with decrease in the distance between the rib and the stagnation point. Due to the highest performance factor up to 1.9 is obtained at the rib height of 0.2 and rib location of 2, therefore the use of nanofluid and triangular ribs can be achieved the best choice of a confined impinging jet over Reynolds number range.

## Nomenclature

| | |
|---|---|
| H | channel height (m) |
| w | jet width (m) |
| L | channel length (m) |
| K | thermal conductivity (W/m.K) |
| Nu | Nusselt number |
| h | heat transfer coefficients (W/m$^2$.$^o$C) |
| P | pressure (pa) |
| $C_p$ | specific heat (J/Kg.K) |
| J | Jacobian of transformation |
| T | temperature ($^o$C) |
| f | friction factor |
| Pr | Prandtl number |
| Re | Reynolds number ($Re=\rho_{nf}\, v_{in}\, w/\mu_{nf}$) |
| U, V | dimensionless velocity component |
| u, v | velocities components (m/s) |
| X, Y | non-dimensional Cartesian coordinates |
| x, y | 2D Cartesian coordinate (m) |

Greek symbols

| | |
|---|---|
| $\beta_{21}$, $\beta_{22}$ | transformation coefficients |
| $\beta_{11}$, $\beta_{12}$ | transformation coefficients |
| η, ζ | body-fitted coordinates |
| μ | dynamic viscosity (N.s/m$^2$) |
| θ | non-dimensional temperature |
| ρ | density (Kg/m$^3$) |
| φ | concentration of nanofluids |
| Δp | pressure drop (pa) |
| κ | Boltzmann constant 1.381 x 10-23 (J/K) |

Subscripts

| | |
|---|---|
| in | inlet |
| n$f$ | nanofluid |
| av | average value |
| e$ff$ | effective |
| p | particles |
| w | wall |
| $f$ | base fluid |
| x | local value |
| bf | base fluid (Water) |

## References


[1] R. Viskanta, "Nusselt-Reynolds Prize Paper Heat Transfer to Impinging Isothermal Gas and Flame Jets," pp. 111–134, 1993.

[2] D. Hee, J. Ryeol, H. Jin, J. Sik, and P. Ligrani, "International Journal of Heat and Mass Transfer Confined , milliscale unsteady laminar impinging slot jets and surface Nusselt numbers," *Int. J. Heat Mass Transf.*, vol. 54, no. 11–12, pp. 2408–2418, 2011.

[3] D. Hee, H. Jin, and P. Ligrani, "International Journal of Heat and Mass Transfer Milliscale confined impinging slot jets : Laminar heat transfer characteristics for an isothermal flat plate," *Int. J. Heat Mass Transf.*, vol. 55, no. 9–10, pp. 2249–2260, 2012.

[4] D. Sahoo and M. A. R. Sharif, "Numerical modeling of slot-jet impingement cooling of a constant heat flux surface confined by a parallel wall," *Int. J. Therm. Sci.*, vol. 43, no. 9, pp. 877–887, 2004.

[5] I. Dagtekin and H. F. Oztop, "Heat transfer due to double laminar slot jets impingement onto an isothermal wall within one side closed long duct," *Int. Commun. Heat Mass Transf.*, vol. 35, no. 1, pp. 65–75, 2008.

[6] K. S. Choo and S. J. Kim, "Comparison of thermal characteristics of confined and unconfined impinging jets," *Int. J. Heat Mass Transf.*, vol. 53, no. 15–16, pp. 3366–3371, 2010.

[7] M. A. R. Sharif, "Heat transfer from an isothermally heated flat surface due to twin oblique slot-jet impingement," *Procedia Eng.*, vol. 56, no. September 2015, pp. 544–550, 2013.

[8] Ş. M. Simionescu, N. O. Tănase, D. Broboană, and C. Bălan, "Impinging Air Jets on Flat Surfaces at Low Reynolds Numbers," *Energy Procedia*, vol. 112, no. October 2016, pp. 194–203, 2017.

[9] A. K. Barik, A. Mukherjee, and P. Patro, "Heat transfer enhancement from a small rectangular channel with different surface protrusions by a turbulent cross flow jet," *Int. J. Therm. Sci.*, vol. 98, pp. 32–41, 2015.

[10] S. V. Ekkad and D. Kontrovitz, "Jet impingement heat transfer on dimpled target surfaces," *Int. J. Heat Fluid Flow*, vol. 23, no. 1, pp. 22–28, 2002.

[11] K. Kanokjaruvijit and R. F. Martinez-Botas, "Heat transfer correlations of perpendicularly impinging jets on a hemispherical-dimpled surface," *Int. J. Heat Mass Transf.*, vol. 53, no. 15–16, pp. 3045–3056, 2010.

[12] G. S. Azad, Y. Huang, and J.-C. Han, "Impingement Heat Transfer on Dimpled Surfaces Using a Transient Liquid Crystal Technique," *J. Thermophys. Heat Transf.*, vol. 14, no. 2, pp. 186–193, 2000.

[13] J. Ortega-Casanova and F. J. Granados-Ortiz, "Numerical simulation of the heat transfer from a heated plate with surface variations to an impinging jet," *Int. J. Heat Mass Transf.*, vol. 76, pp. 128–143, 2014.

[14] C. Gau and I. C. Lee, "Flow and impingement cooling heat transfer along triangular rib-roughened walls," vol. 43, pp. 4405–4418, 2000.

[15] M. M. Dobbertean and M. M. Rahman, "Numerical analysis of steady state heat transfer for jet impingement on patterned surfaces," *Appl. Therm. Eng.*, vol. 103, pp. 481–490, 2016.

[16] O. Manca, P. Mesolella, S. Nardini, and D. Ricci, "Numerical study of a confined slot impinging jet with nanofluids," *Nanoscale Res. Lett.*, vol. 6,

no. 1, pp. 1–16, 2011.
[17] S. J. Palm, G. Roy, and C. T. Nguyen, “Heat transfer enhancement with the use of nanofluids in radial flow cooling systems considerin temperature-dependent properties, ” *Appl. Therm. Eng.*, vol. 26, no. 17–18, pp. 2209–2218, 2006.
[18] Y. T. Yang and F. H. Lai, “Numerical investigation of cooling performance with the use of Al2O3/water nanofluids in a radial flow system,” *Int. J. Therm. Sci.*, vol. 50, no. 1, pp. 61–72, 2011.
[19] B. Sun, Y. Qu, and D. Yang, “Heat transfer of Single Impinging Jet with Cu Nanofluids,” *Appl. Therm. Eng.*, vol. 102, no. March, pp. 701–707, 2016.
[20] I. Gherasim, G. Roy, C. T. Nguyen, and D. Vo-Ngoc, “Experimental investigation of nanofluids in confined laminar radial flows,” *Int. J. Therm. Sci.*, vol. 48, no. 8, pp. 1486–1493, 2009.
[21] O. Manca, D. Ricci, S. Nardini, and G. Di Lorenzo, “Thermal and fluid dynamic behaviors of confined laminar impinging slot jets with nanofluids,” *Int. Commun. Heat Mass Transf.*, vol. 70, pp. 15–26, 2016.
[22] M. A. Ahmed, M. M. Yaseen, and M. Z. Yusoff, “Numerical study of convective heat transfer from tube bank in cross flow using nanofluid,” *Case Stud. Therm. Eng.*, vol. 10, pp. 560–569, 2017.
[23] C. Qi, J. Hu, M. Liu, L. Guo, and Z. Rao, “Experimental study on thermo-hydraulic performances of CPU cooled by nanofluids,” *Energy Convers. Manag.*, vol. 153, no. July, pp. 557–565, 2017.
[24] Y. Xuan and W. Roetzel, “Conceptions for heat transfer correlation of nanofluids,” *Int. J. Heat Mass Transf.*, vol. 43, no. 19, pp. 3701–3707, 2000.
[25] M. Corcione, “Empirical correlating equations for predicting the effective thermal conductivity and dynamic viscosity of nanofluids,” *Energy Convers. Manag.*, vol. 52, no. 1, pp. 789–793, 2011.
[26] R. S. Vajjha and D. K. Das, “A review and analysis on influence of temperature and concentration of nanofluids on thermophysical properties, heat transfer and pumping power,” *Int. J. Heat Mass Transf.*, vol. 55, no. 15–16, pp. 4063–4078, 2012.
[27] H. A. Mohammed, A. N. Al-Shamani, and J. M. Sheriff, “Thermal and hydraulic characteristics of turbulent nanofluids flow in a rib-groove channel,” *Int. Commun. Heat Mass Transf.*, vol. 39, no. 10, pp. 1584–1594, 2012.
[28] Versteeg H.K & Malalasekera, *An Introduction to Computational Fluid Dynamics*, vol. M. 2007.
[29] J. H. Ferziger and M. Peric, *Computational methods for fluid dynamics*, vol. 46, no. 2–3. 2003.